ACERP: Vol. 6, No.3, (Summer 2020) 1-14

Advanced Ceramics Progress

Research Article

Journal Homepage: www.acerp.ir

Effect of Carbide Particle Size on the Microstructure, Mechanical properties, and Wear Behavior of HVOF-sprayed WC-17% Co Coatings

S. M. Nahvi [a] *

[a] *Department of Materials Engineering, Isfahan University of Technology, Isfahan, 84156-83111, Iran*

PAPER INFO

Paper history:

Received 25 April 2020
Accepted in revised form 18 May 2020

Keywords:

WC-Co
HVOF
Microstructure
Mechanical Properties
Abrasive Wear

ABSTRACT

This study investigates the effect of carbide particle size on the microstructure, mechanical properties, and abrasive wear resistance of WC-17%Co HVOF-sprayed coatings. The characteristics of WC-1, WC-2, and WC-3 coatings with carbide sizes of 1 µm, 0.9 µm, and 0.5 µm, respectively, were also investigated. WC-1 coating experienced the maximum carbon loss of 42%, while WC-2 and WC-3 coatings underwent lower carbon losses of 30% and 29%, respectively. The XRD pattern revealed W_2C/WC peak ratios of 15.58, 9.14, and 14.96% for WC-1, WC-2, and WC-3 coatings, respectively. The Vickers microhardness of WC-1, WC-2, and WC-3 coatings was measured as 1418 ± 61, 1306 ± 71, and 1203 ± 57 kgf/mm^2, respectively. The WC-2 coating showed the maximum fracture toughness of 5.9 MPa.m$^{1/2}$, after which WC-3 and WC-1 coatings were characterized by 5.6 and 5.4 MPa.m$^{1/2}$, respectively. The wear rate of the coatings abraded by alumina 60 was 1.2-7.8 times higher than that of the coatings abraded by silica 70 almost over the whole range of applied loads (19.6-127.5 N). The WC-3 coating exhibited lower abrasive wear resistance against alumina 60 than WC-1 and WC-2 coatings. The worn surfaces produced by alumina 60 abrasive showed indications of grooving, pitting, and cutting of the coatings' surfaces. For all coatings abraded by silica 70, removal of the matrix, micro-grooving, carbide particles fragmentation, and voids formation through carbide pullout were detected. For WC-3 coating, in contrast to WC-2 and WC-3, the indications of sub-surface cracking were identified when abraded by both alumina 60 and silica 70.

1. INTRODUCTION

Sintered WC-Co materials consisting of hard WC particles and a ductile cobalt binder phase are extensively utilized in wear-resistant applications such as cutting and machining tools, extrusion dies, etc. due to their excellent combination of high hardness, fracture toughness, and superior wear resistance [1-4]. Due to a decrease in WC particle size on the nanometer scale, the mean free path of cobalt matrix is reduced, thus resulting in greater resistance against deformation and binder phase extrusion. As a result, compared to conventional materials, sintered nanostructured WC-Co materials exhibited higher hardness and greater wear resistance [5-8]. Thermally sprayed WC-Co coatings, mostly deposited by High Velocity Oxygen Fuel (HVOF) spraying, have also received increasing attention and is utilized in numerous applications such as seats and gates in the petroleum industry, as well as copper crystallizers and pinch rolls in the steel industry [9-11]. Researchers have studied the same approach with respect to nanostructured WC-Co coatings; however, the obtained results of the performance of coatings have been controversial to date. In other words, a review of several related studies shows that HVOF-sprayed nanostructured WC-Co coatings outperform conventional WC-Co coatings in terms of their higher hardness, wear resistance, and lower friction coefficient [12-14]. However, other researchers reached a different conclusion [15-18]. Therefore, additional investigations are required in this domain in order to explore a comprehensive study on WC-Co coatings and the relationship among the carbide particle size, mechanical properties, and wear resistance.

In the present study, WC-17%Co powders of three different carbide particle sizes were deposited by HVOF thermal spraying. The effect of carbide particle size on the mechanical properties, microstructure, and abrasive

* Corresponding Author Email: mehran.nahvi@cc.iut.ac.ir (S. M. Nahvi)

https://doi.org/10.30501/acp.2020.227010.1033

wear resistance was evaluated.

2. EXPERIMENTAL PROCEDURES

2.1. FEEDSTOCK POWDERS AND HVOF COATINGS

Three commercial WC-Co powders with different WC particle sizes of 1 (WC-1), 0.9 (WC-2), and 0.5 μm (WC-3) were utilized as HVOF feedstock materials. All powders were agglomerated and sintered spheroids with nominal diameters ranging from 15 to 45 μm. Malvern Mastersizer S (Malvern Instruments Ltd, Worcestershire, UK) laser particle size analyzer was utilized to measure the particle-size distribution of the powders. Table 1 presents the general properties of the powders.

TABLE 1. General properties of WC-Co powders

Powder	Manufacturer	Powder designation	WC size (μm)	Composition (wt%)			
				W	Fe	Co	C
WC-1	H.C. Starck	Amperite 526	1	78.09	0.05	16.83	5.03
WC-2	Sulzer Metco	Woka 3202	0.9	77.97	0.04	16.83	5.16
WC-3	Sulzer Metco	Woka 3202 FC	0.5	77.85	0.03	17.02	5.1

Plain-carbon steel (0.12% C, 0.7% Mn) sheets with dimensions of 59 × 25 × 3 mm and hardness of 241 kgf.mm^{-2} were used as substrates for coating deposition. Prior to HVOF spraying, grit blasting the substrates with ~250 μm brown alumina is required to degrease and roughen the surface. Praxair/UTP Top-Gun HVOF spray system, whose parameters are specified in Table 2, was used to spray the feedstock powders onto the substrates. Hydrogen and nitrogen as the fuel and carrier gases, respectively, were used and the samples were cooled with compressed air jets during spraying.

TABLE 2. Spray parameters employed for coatings deposition

Spray parameter	WC-1	WC-2	WC-3
O_2 flow rate (l min^{-1})	240	240	240
Fuel gas (H_2) flow rate (l min^{-1})	640	640	640
Carrier gas (N_2) flow rate (l min^{-1})	17	17	17
Spray distance (mm)	250	250	250
Number of pass	40	40	40
Length of pass (mm)	77	77	77
Carousel diameter (mm)	280	280	280
Substrate velocity (m s^{-1})	1	1	1
Gun transverse speed (mm s^{-1})	5	5	5
Coating time (s)	733	674	669
Consumption of powder (g)	665	710	711
Coating thickness (μm)	350	445	460
Powder feed rate (g min^{-1})	54	63	63

2.2. MICROSTRUCTURAL CHARACTERIZATIONS

This study used X-Ray Diffraction (XRD) (Siemens D500 diffractometer, 40 kV, 25 mA) to identify the phase composition of the powders and coatings via monochromatic Cu K_α (λ = 0.15406 nm) radiation. The XRD spectra were recorded over a 2θ range of 30°–80° with a step size of 0.010° and 4s dwell time per step.

Scanning Electron Microscope (SEM) (Philips XL30, FEI Ltd.) equipped with energy dispersive X-ray (EDX) analysis was used for microstructural examination of feedstock powders and as-sprayed coatings. SEM observations were carried out at an accelerating voltage value of 20 kV in both Secondary Electron (SE) and Back-Scattered Electron (BSE) modes. Image analysis software (ImageJ 1.41) evaluated SEM/BSE images at a magnification of 2500× to figure out the porosity of the coatings. The mean pore volume fraction was calculated by recording at least ten images. The line analysis method derived from BSE micrographs at magnifications ranging from 5000 to 10000× was utilized to estimate the volume fraction of phases and the carbide particle size of the powders and coatings.

Chemical analysis of as-sprayed coatings by LSM Ltd. (London and Scandinavian Metallurgical Co. Limited, South Yorkshire, UK) was conducted. While XRF-HSS (quantitative) was applied to determine Oxygen and Carbon contents, X-Ray Fluorescence (XRF) technique using XRF-UniQuant (semiquantitative) was used to determine other elements.

2.3. EVALUATION of MECHANICAL PROPERTISE

LECO M-400 microhardness tester was applied in this study to measure Vickers microhardness of as-sprayed coatings under a load of 300 gf at a dwell time interval of 15 s. The coatings' hardness is described as the average value of 10 indents taken along the mid-plane of the cross-section parallel to the coating/substrate interface.

An indentation method was utilized to measure the coatings' fracture toughness. To this end, Vickers indentation measurements were performed on the metallographically prepared cross-sections of the coating under a load of 5 kgf. The image analysis software (ImagJ 1.41) was also utilized to measure the length of cracks parallel to the substrate/coating interface via optical micrographs at a magnification of 400×. At least 35 indentations were conducted for each coating. The model proposed by A.G. Evans and T.R. Wilshaw was considered to calculate the coatings' fracture toughness (*K*c) [19]:

$$K_C = 0.079 \left(\frac{P}{a^{3/2}}\right) log\left(\frac{4.5a}{c}\right) \quad (1)$$

where P is the applied indentation load (N), a is the indentation half diagonal (m), and c is the crack length from the center of the indent (m). The recommended c/a ratio for valid use of this equation is $0.6 \leq c/a < 4.5$.

2.4. ABRASIVE WEAR TESTING

To carefully study the coatings' behavior under three-body low stress-abrasion conditions, Dry Sand Rubber Wheel (DSRW) test was applied to test the samples. As shown in Fig. 1, the coating sample is held in a slot at the top of the rotating wheel to control the feed of abrasive to be passed between the wheel and the sample.

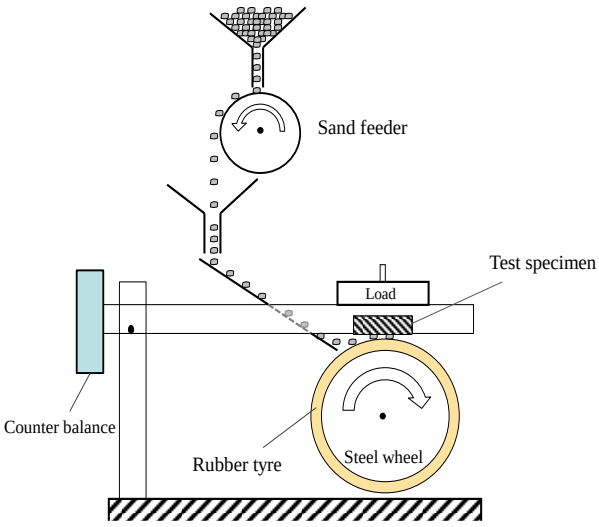

Figure 1. Schematic representation of dry sand rubber wheel abrasion test apparatus

The rubber wheel made of a polyurethane cast elastomer (monothane A60; CIL, Preston, UK) was coated around an inner steel wheel to increase the total diameter to 227 mm. According to Wallace Hardness Meter, the width and international rubber hardness of the tyre were 12 mm and 63 ± 3 degrees, respectively. The rotation speed of the rubber was set at 195 rpm, equivalent to the sliding speed of 2.32 m s^{-1} and in agreement with ASTM standard G65.

This study used two groups of abrasives: (a) angular alumina 60 (Abrasive Developments, Henley-in-Arden, UK) in a size range of 212 to 300 μm and sand feed rate of 2.64 g s^{-1}, and (b) rounded silica 70 (The David Ball Company, Bar Hill, UK) in the size range of 180 to 250 μm and sand feed rate of 2.37 g s^{-1} (Fig. 2). The LECO M-400 micro hardness tester at load hardness of 300 gf was used to measure the hardness of the abrasive particles. Abrasive particles were mounted on a hot hardening resin and, then, polished in order to keep the flat cross-section of the particles exposed to indentation. The reported hardness is the average of 5 indents taken from different regions. The Vickers hardness rates of silica 70 and alumina 60 abrasives assessed in the polished cross-sections with an indentation load of 300 gf were 1116 ± 47 kgf.mm^{-2} and 2103 ± 25 kgf.mm^{-2}, respectively.

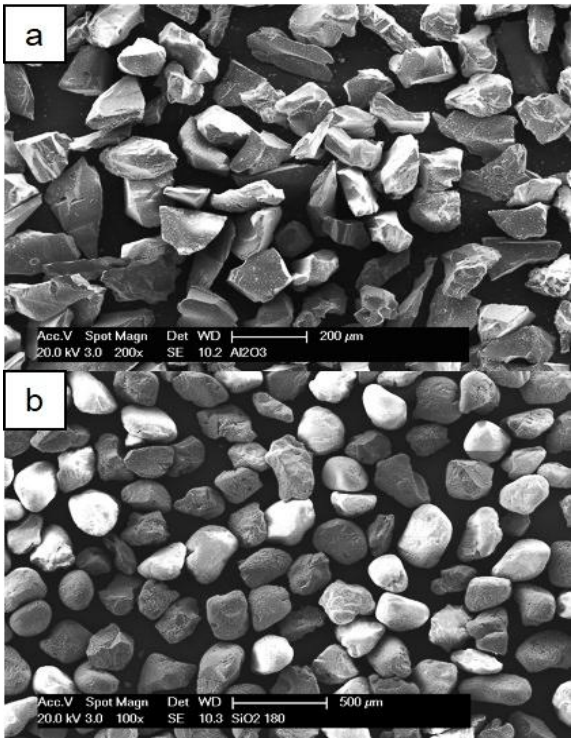

Figure 2. SEM images of (a) alumina 60 and (b) silica 70 abrasive particles

The wear experiments were carried out under the applied loads of 19.6, 49, 98, and 127.5 N. The abrasive particles were fed via a chute towards the rubber wheel just before the contact region between the test specimen and the wheel.

Before and after each test, the coatings' loss of mass was assessed through a GF-200 balance (A&D Instruments Ltd., Tokyo, Japan) with capacity and accuracy of 10g and 0.001 g, respectively. Prior to calculating the wear loss, the coating samples were washed in methanol and, then, dried. For the coating samples, the abrasion distances were 800, 1600, 2400, 3200, and 4000 revolutions. The wear rate was obtained from the slope of the steady state part of the mass loss versus sliding distance graph.

The wear mechanisms were studied by observing the worn surface of the coating samples using Scanning Electron Microscopy (SEM) (Philips XL30, FEI Ltd, Cambridge, UK) with an accelerating voltage of 20 kV

in Secondary Electron (SE) and Back-Scattered Electron (BSE) imaging modes.

3. RESULTS

3.1. MICROSTRUCTURE OF FEEDSTOCK POWDERS AND HVOF COATINGS

The XRD patterns of WC-1, WC-2, and WC-3 powders (Fig. 3) show the main peaks corresponding to WC phase and small peaks related to Co matrix. The XRD patterns reveal no additional carbide phase such as W_2C indicating that all the tungsten content in the starting powders exists in the form of WC phase.

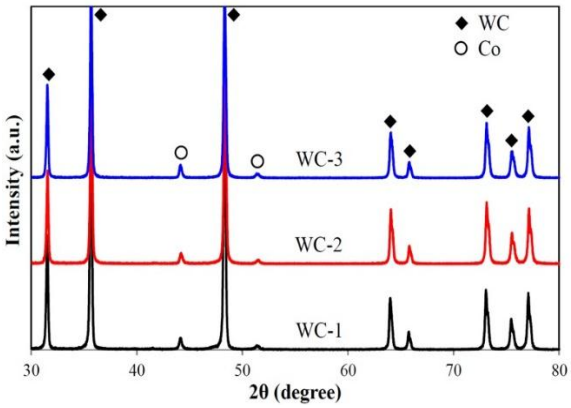

Figure 3. XRD patterns of starting WC-1, WC-2, and WC-3 powders

Fig. 4 shows the SEM images from morphology and cross-section of WC-1, WC-2, and WC-3 powders. It is evident that the agglomerated and sintered particles possess a spherical morphology and a highly porous structure.

The results of the analysis conducted on the particle size distribution of different powders (Fig. 5), derived from laser diffractometry technique, reveal deviations from the size range and average size of particles in a way that WC-1 and WC-2 powders indicate the minimum and maximum $d_{50\%}$ of 32 and 38 µm, respectively.

Table 3 presents the particle size and volume fraction of WC phase calculated according to the cross-sectional BSE images of the powders through the line analysis method. Moreover, given the assumption that WC and Co densities are 15.63 g.cm^{-3} [22] and 8.90 g.cm^{-3}, respectively, Table 3 shows the calculated volume fraction of WC based on the mass fractions claimed by the manufacturers. The results obtained from the calculated volume fraction of WC phase are in good agreement with each other, which verifirs their accuracy.

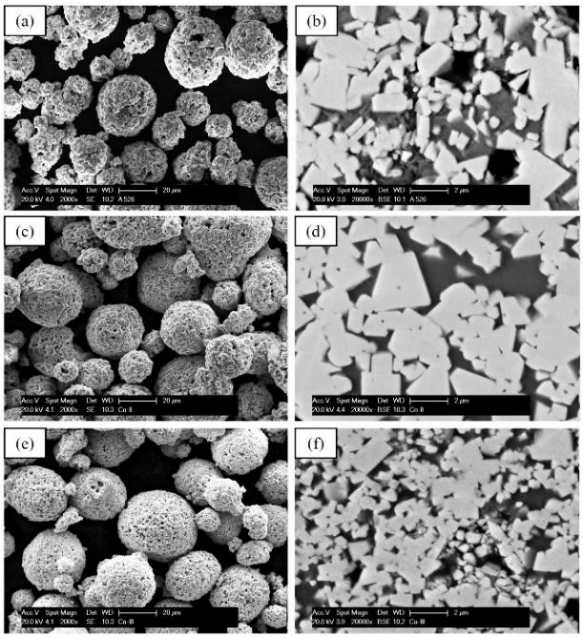

Figure 4. SEM images from morphology and cross-section of (a,b) WC-1, (c,d) WC-2, and (e,f) WC-3 powder particles

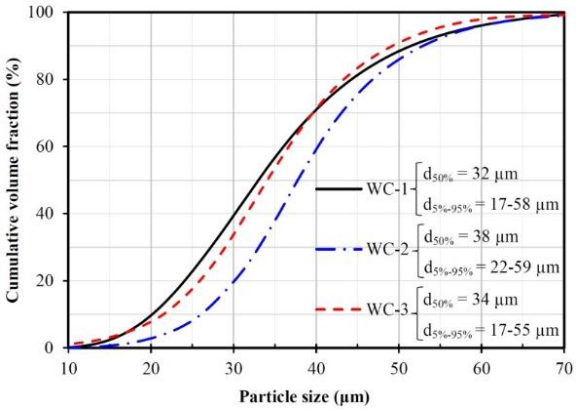

Figure 5. Particle size analysis of WC-1, WC-2, and WC-3 powder particles

TABLE 3. Particle size and volume fraction of WC in the powders measured via line analysis and calculated from the chemical composition of the powders

Powder	Measured volume fraction of WC (%)	Calculated volume fraction of WC (%)	WC particle size (µm)
WC-1	72	74	1.0
WC-2	67	74	0.9
WC-3	71	73	0.5

Table 4 presents the chemical composition, carbon loss, and (W_2C/WC) peak ratio of as-sprayed coatings. Obviously, for all coatings, significant carbon loss during HVOF spraying was observed. While WC-1 coating experienced the highest rate of carbon loss (42%), WC-2 and WC-3 coatings underwent lower rates, i.e., 30% and 29%, respectively.

Fig. 6 shows the comparative XRD patterns of WC-1, WC-2, and WC-3 coatings sprayed under the conditions specified in Table 2.

TABLE 4. Chemical composition, carbon loss, and (W_2C/WC) peak ratio for different coatings

Coating	Composition (wt%)				Carbon loss (%)	XRD peak height ratio (W_2C/WC)×100
	W	Fe	Co	C		
WC-1	79.90	0.05	17.16	2.89	42	15.58
WC-2	79.26	0.04	17.09	3.61	30	9.14
WC-3	79.05	0.03	17.29	3.63	29	14.96

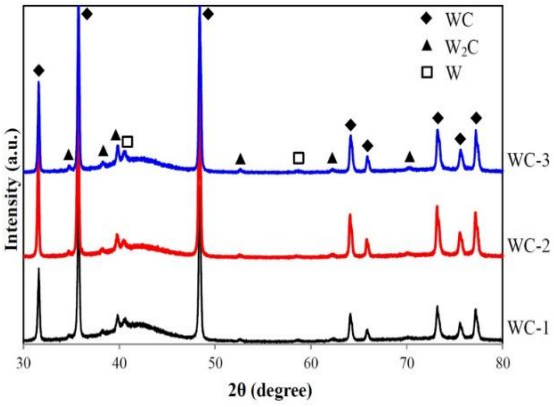

Figure 6. XRD patterns of as-sprayed WC-1, WC-2, and WC-3 coatings

According to the observations, all types of coating experience WC decarburization during HVOF spraying. However, the levels of WC decarburization are different. When WC-1, WC-2, and WC-3 powder particles are exposed to high-temperature HVOF flame (~3000 °C), Co matrix melts upon which WC particles begin to dissolve into the liquid Co. The oxidizing atmosphere of HVOF flame makes a portion of dissolved Carbon oxidized in the form of CO/CO_2 gas mixture that finally leads to decarburization. Some of the remaining dissolved W and C are recrystallized as W_2C and W phases in the solidification process and the rest are kept in the binder to form W-rich Co matrix [23-25]. For all coatings, XRD peaks that correlate with W_2C and W phases formed during deposition are detected. A broad diffraction halo between 2θ values of approximately 37 and 47° for each coating is found, suggesting that there is an amorphous phase in the deposits. Moreover, the coatings' XRD patterns show no crystalline peaks corresponding to the Co binder phase. The analysis of XRD pattern reveals that the W_2C/WC peak ratios of WC-1, WC-2, and WC-3 coatings are 15.58, 9.14, and 14.96% , respectively. According to Table 2, the spray parameters for all coatings were nearly the same; therefore, the powder's particle size is likely the reason why the levels of decarburization are different. In other words, the smaller the particle size is, the higher the temperature reached by the powder particles leading to the larger extent of WC decarburization. According to the aforementioned findings, one can conclude that the maximum carbon loss and W_2C/WC ratios of WC-1 coating (42% and 15.58%, respectively) are highly dependent on its smaller particle size (32 µm), compared to WC-2 (38 µm) and WC-3 (34 µm). However, this trend is not observed when comparing WC-2 and WC-3 coatings. In comparison with WC-2 with the particle size, carbon loss, and W_2C/WC ratio of 38 µm, 30%, and 9.14%, respectively, WC-3 with the particle size of 34 µm shows almost the same carbon loss (29%), but a higher W_2C/WC ratio (14.96%). This implies that at the same rate of carbon loss, the amount of W_2C phase varies depending on the WC particle size. Given the reduction of the size of WC from 0.9 µm for WC-2 to 0.5 µm for WC-3, W_2C/WC ratio increases from 9.14 to 14.96%. It can be suggested that at the same level of decarburization, smaller WC particles stimulate the formation of W_2C phase upon solidification by acting as more effective nucleation sites for W_2C precipitation than the larger WC particles. Fig. 7 illustrates the BSE images of cross-section of WC-1, WC-2, and WC-3 coatings.

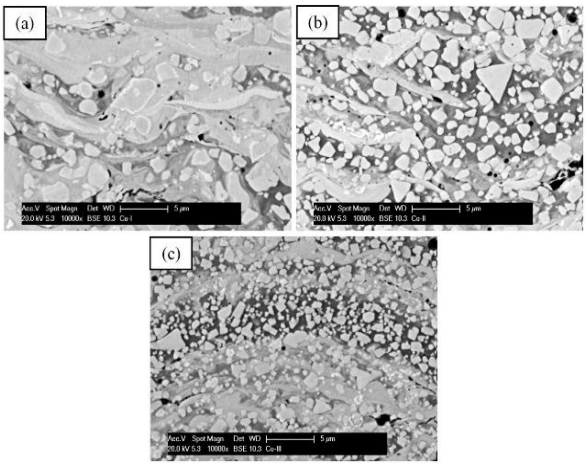

Figure 7. BSE images of cross-section of (a) WC-1, (b) WC-2, and (c) WC-3 coatings

The above images demonstrate splat-like microstructures of thermal spraying characterized by bright and dark contrast matrix layers that correspond to the areas containing higher and lower average atomic numbers, respectively. Angular WC particles are visible within the darker regions of all coatings, whereas WC particles are round in shape and are fully or partially enclosed by an irregular bright fringe identified as W_2C phase in the brighter areas [26,27]. Different dissolved W levels primarily give rise to different contrast levels of the matrices. Even though the size of the shells that cover WC particles prevents precise SEM/EDS, they clearly possess considerably lower carbon levels than the particle centers. Therefore, W_2C and W phases as identified by XRD are likely to be the shells that cover WC particles. As shown in Fig. 7a, the microstructure of WC-1 coatings is characterized by a large extent of amorphous (high tungsten) binder phase in which rounded WC particles mostly surrounded by W_2C phase are evident.

After that, WC-3 (Fig. 7c) coating reveals the highest level of amorphous binder phase with bright contrast in which smaller WC particles partly enclosed by W_2C are randomly distributed. As for WC-2 coatings, WC particles of angular morphology are distributed in a darker binder phase and more limited evidence of W_2C phase is observed than WC-1 and WC-3 coatings. This finding can be ascribed to the larger sizes of WC-2 particles (38 µm) that lead to their lower heating during spraying and, consequently, a lower W_2C/WC ratio (9.14%) than other coatings.

The metallographic technique of line analysis was employed to measure mean diameter of WC particles and volume fraction of the binder on the all coating cross-sections. Then, the following equation was used to measure the mean free path of the binder (λ) based on BSE images [28]:

$$\lambda = \frac{(1-f)}{N_L} \qquad (2)$$

where N_L represents the number of discontinuous particles which are converged on a metallographic plane by a line of unit length and *f* is the volume fraction of the dispersed phase. In the case of every coating, the average of five measurements was reported. Table 5 presents the average volume fraction of binders, WC particle size, and mean free path of the binders for all coatings.

The results indicate that WC-1 coating is characterized by the lowest carbide phase amount and the highest mean free path value, while these values specific to WC-2 and WC-3 coatings are comparable. Table 6 presents WC particle size and carbide volume fraction of both powders and coatings.

It is obvious that the most significant change in volume fraction of carbide phase takes place during spraying of WC-1 (51%), while WC-2 by 18% exhibits the minimum change in the carbide phase volume faction. Furthermore, the carbide particle size varied by -10%, 11% upon spraying of WC-1 and WC-2 coatings, whereas the changes in carbide particle size of WC-3 were negligible. The image analysis of BSE images of the coatings was taken into account to calculate their porosity. Figure 8 represents the typical images of the coating's cross-section followed by the coatings' porosity analysis.

TABLE 5. Volume fraction of carbide, WC particle size, and mean free path of the binders for WC-1, WC-2, and WC-3 coatings derived from line analysis method

Coating	Volume fraction of WC (%)	WC particle size (µm)	Mean free path (µm)
WC-1	35	~1.1	2.03
WC-2	55	~0.8	0.68
WC-3	49	~0.5	0.54

TABLE 6. Comparison of volume fractions and particle size of carbide in the powder and coating

Coating	Carbide phase volume fraction (%)			Size of carbide particle (µm)		
	Powder	Coating	Changes	Powder	Coating	Changes
WC-1	72	35	51 %	1.0	1.1	-10 %
WC-2	67	55	18 %	0.9	0.8	11 %
WC-3	71	49	33 %	0.5	0.5	0 %

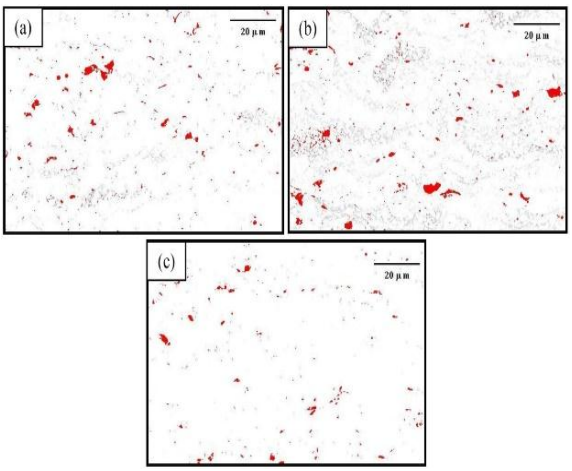

Figure 8. Image analysis performed on the cross-sectional BSE images of (a) WC-1, (b) WC-2, and (c) WC-3 coatings

Table 7 indicates the volume fraction of the porosity together with the average pore size of the coatings. According to the findings, the porosity levels of WC-1, WC-2, and WC-3 coatings are quite limited (< 1.8 vol%) due to the high degree of melting and uniform plastic flow of splats upon impact to the substrate. WC-1 and WC-3 coatings reveal the maximum and minimum average pore sizes of 0.27 and 0.42 µm, respectively.

TABLE 7. Porosity percentage and mean pore size measured by image analysis of the cross-sectional BSE images of the coatings

Coating	Average pore size (µm)	Porosity (vol %)
WC-1	0.27	1.6
WC-2	0.36	1.8
WC-3	0.42	1.2

3.2. MECHANICAL PROPERTISE OF THE COATINGS

The measured Vickers microhardness of WC-1, WC-2, and WC-3 coatings was 1418 ± 61, 1306 ± 71, and 1203 ± 57 kgf/mm^2, respectively. While the hardness of WC-3 was found to be the lowest, that of WC-1 coating was the highest. The hardness of thermally sprayed WC cermet coatings is highly dependent on the following criteria: the volume fraction of retained hard WC phase, volume fraction of new phases (e.g., W_2C and W), hardness of the binder phase, and microstructural properties of the coating (i.e., porosity, mean free path of binder, and WC particle size). The retained carbide phase plays a key role in assessing the hardness of the thermally sprayed WC cermet coatings. In this respect, considerable attempts have been made to take control over the decomposition of the carbide phase during the spraying process. According to the relevant investigations, the hardness of WC cermet coatings increases through decreasing decomposition [29,30]. Usmani et al. [31] suggested that upon an increase in the W_2C content, the hardness of the coating decreased. The formation of a more brittle W_2C phase around the WC particles reduces the WC-matrix cohesion and, consequently, deteriorates the mechanical properties including hardness [32,33].

On the contrary, the larger the extent of WC decarburization during spraying is, the more enriched the binder phase in W and C will be. This happens due to the high solubility of these elements in the binder phase during rapid solidification [34]. Moreover, the hardness and brittleness of coatings are enhanced as a result of this enrichment. Although decarburization lessens the volume fraction of WC phase, its damaging impact on the hardness is compensated through hardening the cobalt matrix during the dissolution process of W and C into the binder phase [35]. WC-1 coating owes its maximum hardness of 1418 ± 61 kgf/mm^2 to this enrichment. In fact, compared to WC-2 and WC-3 coatings, the highest decarburization (42%) and low WC fraction signify considerable enrichment of the binder phase in both W and C that guarantees an increase in the hardness.

Despite approximately the same decarburization degree of WC-2 and WC-3 coatings, their hardness is different from each other. According to the data given in Table 6, the volume fraction of carbide in WC-2 (55%) is higher than that of WC-3 (49%); however, the lower W_2C/WC ratio in the former (9.14%) verifies more retained WC phase in the coating's microstructure. This is why WC-2 exhibits shows greater hardness than WC-3 coating.

Evans and Wilshaw's Equation was used to calculate the coatings' fracture toughness through measuring the Vickers indentations under a vertical load of 5 kgf. For each coating, the measured fracture toughness ranged orderly from low toughness (long cracks) to high toughness (short cracks). In the light of this approach, Fig. 9a presents the cumulative distribution of fracture toughness for different coatings.

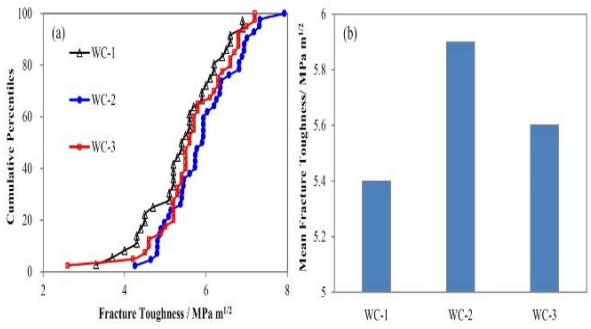

Figure 9. (a) Cumulative percentiles and (b) mean values of indentation fracture toughness for WC-1, WC-2, and WC-3 coatings

As shown in Fig. 9a, the cumulative percentile versus fracture toughness shows a very similar variation for different coatings. Fig. 9a confirms that WC-2 coating has the maximum mean fracture toughness of 5.9 MPa.m$^{1/2}$; WC-3 and WC-1 coatings show lower values of 5.6 and 5.4 MPa.m$^{1/2}$, respectively. The lower fracture toughness of WC-1 coating than that of other coatings results from the larger extent of decarburization (42%), amorphous binder phase formation (see Fig. 7a), and higher W_2C/WC ratio (15.58%). It is well established that the amorphous W-rich binder phase, embrittled by WC dissolution, is the preferential path for crack propagation, thereby deteriorating the coatings' fracture toughness [36-38]. In addition, large amount of

W_2C phase precipitated in the vicinity of WC particles for WC-1 coating weakens the cohesion of WC-binder interface enabling the initiation and propagation of cracks on the coating [39]. Although WC-2 and WC-3 coatings undergo the same decarburization level, the lower W_2C/WC ratio in the former (9.14%) accounts for its greater fracture toughness.

3.3. THE COATINGS' ABRASIVE WEAR

The Dry Sand Rubber Wheel (DSRW) testing was implemented to calculate the coatings' abrasive wear by means of alumina 60 and silica 70 abrasives under four different loads of 19.6, 49, 98, and 127.5 N, respectively. The least squares fit of the data in the linear (steady state) regime determines the wear rate. Fig. 10 represents the rates of steady state wear with alumina 60 and silica 70 abrasives for each type of coating as a function of load.

WC-1 coating abraded by alumina 60 shows a marginal increase in wear rate from 0.0245 to 0.0417 mg.m^{-1} as the applied load rises in the range of 19.6 to 127.5 N. A slightly higher wear rate with maximum amount of 0.054 mg.m^{-1} was obtained for WC-2 coating abraded by alumina 60 under the load of 49 N. On the contrary, the wear rate of WC-3 coating, in comparison to WC-1 and WC-2 coatings, shows a significant increase from 0.0628 to 0.191 mg.m^{-1} with the applied load ranging from 19.6 to 127.5 N, which suggests lower abrasive wear resistance against alumina 60.

The wear rate of WC-1 coating abraded by silica 70 particles increases in the range of 0.0091 to 0.0327 mg.m^{-1} with an increase in the applied load from 19.6 to 98 N; this is followed by a drop in the wear rate to 0.0239 mg.m^{-1} at the load of 127.5 N. The wear rate of WC-2 coating constantly increases from 0.0114 to 0.0449 with the applied load of up to 98 N, reaching a plateau with further load increase to 127.5 N. Finally, the wear rate of WC-3 coating shows an increasing linear trend ranging from 0.016 to 0.0415 mg.m^{-1} with the applied load rising from 19.6 to 127.5 N. As shown in Fig. 10c, the wear rate of the coatings abraded by alumina 60 is ~1.2-7.8 times higher than that of coatings abraded by silica 70 almost over the whole range of the applied load. The wear rate is sensitive to the ratio of abrasive hardness H_a to the surface hardness H_s. Abrasion under $H_a/H_s > 1.2$ and $H_a/H_s < 1.2$ conditions can be termed as "hard abrasion" and "soft abrasion", respectively [40]. Fig. 11 illustrates the H_a/H_s values for each coating-abrasive combination. It is observed that the abrasive wear by silica 70 is located in the "soft" regime, while abrasion by alumina 60 imposes "hard" regime on all coatings.

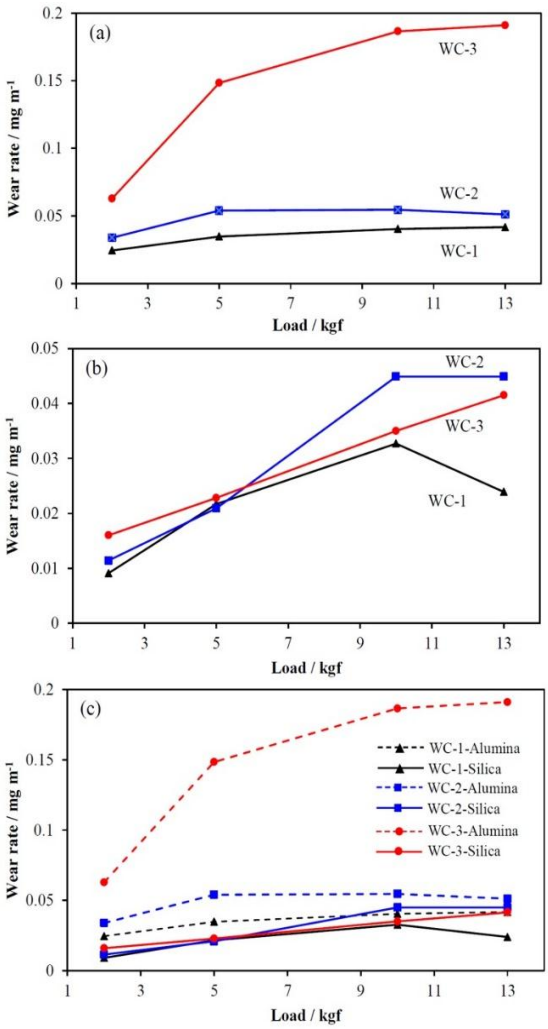

Figure 10. Plots indicating wear rates of WC-1, WC-2, and WC-3 coatings abraded by (a) alumina 60 and (b) silica 70 under different loads; (c) Comparison of the wear rates of the coatings abraded by alumina 60 and silica 70

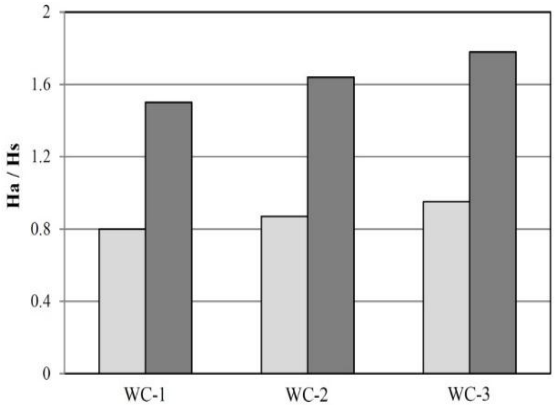

Figure 11. A plot indicating transition between "hard" and "soft" abrasive wear mechanisms ($\frac{H_a}{H_s} = 1.2$) for the coatings abraded by silica 70 and alumina 60

Following wear testing, the central zone of the worn surfaces abraded under minimum and maximum applied loads was examined by SEM. Fig. 12 a,b shows the plan-view SEM images of WC-1 coating abraded by alumina 60 under the loads of 19.6 and 127.5 N, respectively. In both cases, two areas with high and low densities of carbides are apparently separated. Moreover, the wear track formed at the applied load of 19.6 N shows evidence of grooving, carbide cracking and voids; the latter is caused by carbide pull-out. These features become more notable at the load of 197.5 N, leading to the formation of some small pits. The carbide cracking and pull-out are also obvious in the cross-sectional view of WC-1 worn surface (Fig. 12c), while no evidence of subsurface cracking can be observed. Fig. 12 d,e illustrates the plan-view images of wear scar of WC-1 coating after abrasion with silica 70 under the minimum (19.6 N) and maximum (127.5 N) applied loads. The worn surfaces appearing at both loads suggest that the matrix is removed at a higher rate, leaving the exposed carbide particles as well as carbide cracking and pull-out that are of significance at higher loads. Although the cross-sectional SEM image taken at the highest load (Fig. 12f) reveals no significant subsurface cracking, it indicates that the carbide particles are standing proud of the matrix signifying the preferential wear of the matrix phase.

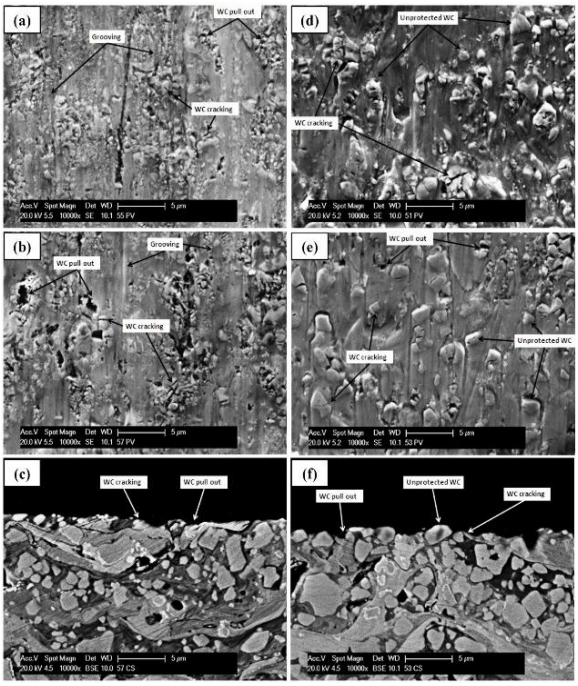

Figure 12. Plan-view SEM images of wear scar of WC-1 coating abraded by (a,b) alumina 60 and (d,e) silica 70 at the loads of 19.6 and 127.5 N, respectively. Cross-sectional SEM images of wear scar of WC-1 coating abraded by (c) alumina 60 and (f) silica 70 at the load of 127.5 N

Fig. 13 a,b shows the SEM images of the WC-2 coating after abrasion with alumina 60 at the loads of 19.6 and 127.5 N, respectively. Carbide pull-out voids and a number of furrows are detected after the matrix removal. Cracked carbides and higher density of voids are observed at higher loads. While no subsurface cracking takes place during abrasion testing of WC-2 by alumina 60, the cross-section of the worn surface (Fig. 13c) confirms WC pull-out and cracking. Plan-view SEM images of wear scars of WC-2 coating after abrasion with silica 70 at the minimum (19.6 N) and maximum (127.5 N) applied loads are presented in Fig. 13 d,e. These wear scars are characterized by three different criteria: 1) regions densely occupied by carbide particles, 2) regions less occupied by carbide particles, and 3) dark regions appearing as carbide pull-out voids. At higher loads (Fig. 13e), some carbides' cracking and a number of furrows are observed as a result of matrix removal. The matrix removal, by itself, results in leaving the carbides unprotected and making them more susceptible to pull-out mechanism during abrasion. Cross-sectional SEM image of worn surface of WC-2 coating abraded by silica 70 (Fig. 13f) shows no sub-surface cracks.

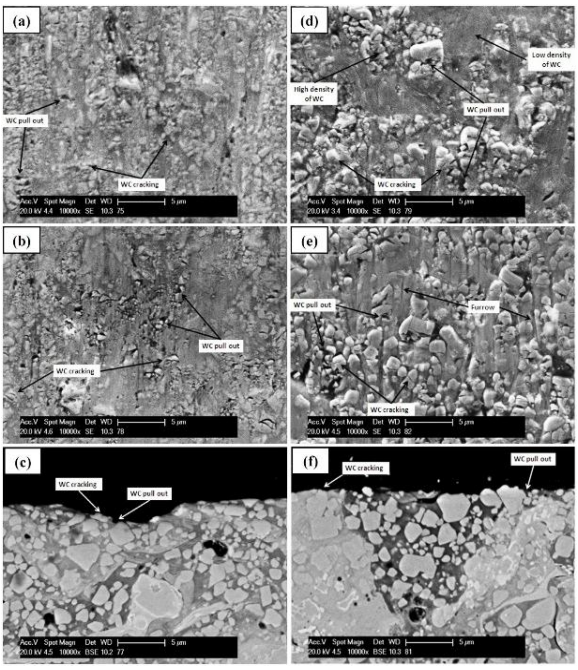

Figure 13. Plan-view SEM images of wear scar of WC-2 coating abraded by (a,b) alumina 60 and (d,e) silica 70 under 19.6 and 127.5 N, respectively. Cross-sectional SEM images of wear scar of WC-2 coating abraded by (c) alumina 60 and (f) silica 70 under 127.5 N

Fig. 14 a,b demonstrates SEM images of the WC-3 coating after abrasion by alumina 60 at minimum (19.6 N) and maximum (127.5 N) applied loads. Two different regions having high and low densities of carbides are evident at both loads. In addition, under 19.6 N load (Fig. 14a), many scratches and some narrow grooves in different directions can be detected, while at the highest applied load (Fig. 14b), wide and deep grooves along the direction of sliding flow are visible. The cross-sectional image of the worn surface under the highest load (Fig. 14c) presents sub-surface cracking with cracks running through the bright binder phase region. Fig. 14.d,e shows images of the central zone of the wear scar on WC-3 coating followed by abrasion with silica 70 at the lowest (19.6 N) and the highest (127.5 N) applied loads, respectively. The wear scars comprise areas with high and low densities of carbides accompanied by a small number of voids caused by carbide pull-out. Further, a number of furrows on the sides of carbide particles because of the removal of matrix at higher rates are visible. The worn surface cross-section after wear at the highest load (Fig. 14f) reveals sub-surface cracks propagating through the bright binder phase. Further, unshielded carbide particles due to preferential wear of the binder phase are apparent on the surface.

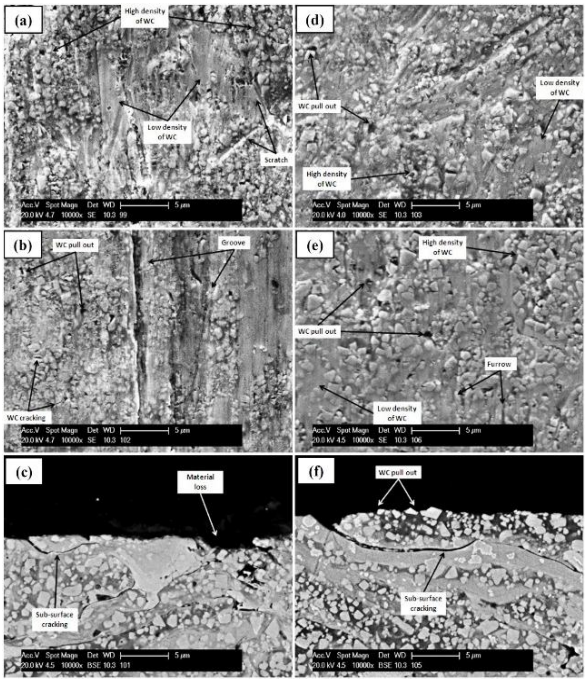

Figure 14. SEM images of wear scar of WC-3 coating abraded by (a,b) alumina 60 and (d,e) silica 70 under 19.6 and 127.5 N, respectively. Cross-sectional SEM images of wear scar of WC-3 coating abraded by (c) alumina 60 and (f) silica 70 under 127.5 N

4. DISCUSSION

4.1. WEAR MEASUREMENTS

The abrasive wear rate of the coatings generally increases with the applied load during abrasion by both alumina 60 and silica 70 (see Fig. 10). However, there are several exceptions for WC-2 abraded by alumina 60 and for WC-1 and WC-2 abraded by silica 70 so that with increasing the applied load to 127.5 N load, the wear rate reveals either unchanged or lower values. This arises from the fact that in DSRW test, the temperature of both sample and wheel increases, the degree of which under a given test parameter depends on abrasive type, sample materials, and applied load [41]. Increasing the rubber temperature as a result of higher load leads to its lower hardness; accordingly, the wear rate decreases in some cases as the applied load increases to 127.5 N [42]. The ratio of abrasive particle hardness to coating hardness shows that for all coatings, the abrasive wear by alumina is "harder" than that by silica which is "soft" (Fig. 11). For all the coatings and test conditions examined, the wear rate by silica 70 particles is significantly lower than that by alumina 60. The worn surface examination verifies that almost in all cases, silica 70 abrasive shows evidence of the preferential cobalt matrix abrasion followed by carbide cracking and pull-out, while alumina abrasive imposes more severe carbide cracking and pull-out together with grooving along the direction of abrasive flow. Increasing the applied load faciliates the formation of deeper grooves. Further, pieces of evidence of subsurface cracking are observed for WC-3 coating abraded by both silica 70 and alumina 60 abrasives. The angular morphology and higher hardness of alumina than those of more rounded silica particles result in significant differences in wear behavior of the coatings.

Fig. 15 displays the wear rate of WC-1, WC-2, and WC-3 coatings as a function of the coating hardness.

The results confirm that the wear rate of the coatings abraded by silica 70 does not necessarily decrease with increasing the coatings' hardness; for instance, WC-2 coating abraded by silica 60 under 98 and 127.5 N shows a higher rate of wear than WC-3 coating, although the former is subject to higher hardness. This originates from the complicated mechanism of abrasive wear in thermally sprayed cermet coatings and importance of parameters other than coatings hardness, e.g., type of abrasive, fracture toughness of the coatings, applied load during DSRW testing, etc.

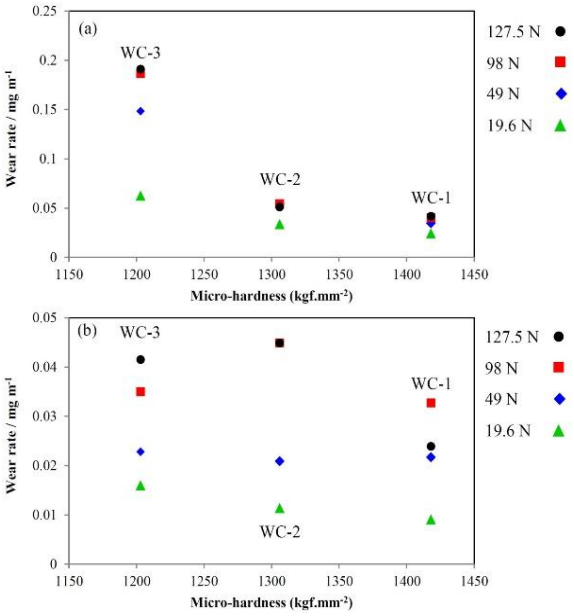

Figure 15. Wear rate versus microhardness plots of WC-1, WC-2, and WC-3 coatings abraded by (a) alumina 60 and (b) silica 70 abrasives

4.2. ABRASIVE WEAR WITH ALUMINA

The hardness of alumina 60 particles (2103 ± 25 kgf.mm^{-2}) is higher than that of all the three coatings examined. These abrasive particles exhibit an angular morphology and a narrow size range (Fig. 2b). Moreover, as plotted in Fig. 11, the ratios of abrasive hardness (H_a) to the hardness of the coatings' surface (H_s) for all coatings are higher than 1.2, demonstrating the role of "hard wear" mechanism. These conditions are conducive to plastic deformation that occurs mostly by plastic ploughing, cutting followed by some local associated fracture in the more brittle cermet coatings [43].

The worn surfaces produced by alumina abrasive show indications of grooving, pitting, and cutting of the coatings' surface. Based on cross-sectional examinations, abrasive wear of WC-3 coating is accompanied by subsurface cracking.

These results show that the two main wear mechanisms, namely plastic deformation and fracture, play a role in material removal. The passage of hard and sharp abrasive facilitates plastic deformation of the surface, leading to the formation of grooves with materials piling up at the groove's edges at the first stage. At the second stage, due to the preferential elimination of the cobalt binder phase, the support is no longer present for carbide particles, leaving them unshielded against the collision of abrasives and leading to both carbides fracture and their pull-out from matrix during abrasive wear. The comparison of the wear rates of the three coatings indicate the highest, medium, and the lowest abrasion resistance rates of WC-1, WC-2, and WC-3 coatings. Considering that the difference in fracture toughness of the coatings is inconsiderable (varying between 5.4-5.9 MPa.m$^{1/2}$ as shown in Fig. 9), it is proposed that the overall hardness of the coatings controls the rate of abrasion by alumina 60; in other words, the higher the coating's hardness, the higher the resistance against alumina 60 abrasive particles. As for WC-3 coating, besides carbides fracture and pull-out, subsurface cracking caused by fatigue of the surface layers leads to the spallation type of failure (see Fig. 14c). As a result, the high-level removal of materials takes place for WC-3 coating resulting in the higher wear rate than the wear rate of WC-1 and WC-2 coatings abraded in the same conditions.

4.3. ABRASIVE WEAR WITH SILICA

The hardness of silica 70 particles (1116 kgf.mm^{-2}) is lower than that of all three coatings examined. These abrasives are characterized by a round morphology and a narrow size range (Fig. 2a). Abrasive hardness (H_a) to the hardness of coatings' surface (H_s) ratio of all coatings is lower than 1.2 indicating "soft wear" regime and, as such, particle blunting is likely to occur during abrasion resulting in a lower wear rate under a three-body (rolling) abrasion mechanism than the wear rate of harder alumina 60 abrasive particles. As proposed in Ref [44], the removal of selective binder phase from the near-surface layers is a significant step in the wear process of cermet materials by soft abrasives. Cyclic indenting contact of abrasive particles during a three-body abrasion process leads to compressive stresses on the coatings' surface. Therefore, the binder is initially compressed out of the surface ahead of and to the sides of the indenter. The next stage is damage to carbide particles located in the heavily loaded regions in which the binder phase has plastically flowed. Hence, carbide particles are exposed to fracture into small fragments and are gradually pulled off the surface.

Cross-sectional examination of WC-3 worn surface abraded by silica 70 (Fig. 14f) confirms that sub-surface cracks mostly propagate through W-rich binder phase of this coating, while no significant evidence of this type of cracking can be observed for WC-1 and WC-2 coatings. Elastic-plastic indentation of the abrasive, facilitating the formation of sub-surface crack close to the WC-3 coating's surface, leads to the detachment of the surface material [45].

As illustrated based on the SEM images of wear scars on all coatings, it can be seen that the metal matrix is abraded at a higher rate, leaving carbides unprotected on the surface. For all coatings, removal of matrix is more pronounced at higher applied loads with micro-grooves being formed by the sides of the carbide particles and,

also, a number of fragmented carbide particles and voids due to the pulling out of the carbides.

A comparison of the wear rates of WC-1, WC-2, and WC-3 coatings shows a similar trend until high applied loads (98 and 127.5 N) are reached. WC-1 with the largest carbide particles and the lowest WC volume fraction (owing to the high degree of decomposition during spray process) shows maximum resistance against silica 70 abrasive, probably because of its higher overall hardness than other coatings. The high hardness of thermally sprayed composite carbide with relatively low carbide content results from the high hardness of the brittle amorphous phase formed after spraying. The higher hardness of the binder phase in an abrasion wear test makes its preferential wear quite limited, leading to a reduction in the wear rate [46,47].

5. CONCLUSIONS

1) The highest carbon loss was measured for WC-1 (42%), while lower values of 30% and 29% were obtained for WC-2 and WC-3 coatings, respectively.
2) The Vickers microhardness of WC-1, WC-2, and WC-3 coatings was calculated as 1418 ± 61, 1306 ± 71, and 1203 ± 57 kgf/mm^2, respectively.
3) WC-2 coating had the maximum fracture toughness of 5.9 MPa.m$^{1/2}$, after which WC-3 and WC-1 coatings showed lower values of 5.6 and 5.4 MPa.m$^{1/2}$, respectively.
4) The wear rate of the coatings abraded by alumina 60 was ~1.2-7.8 times higher than that of the coatings abraded by silica 70 almost over the whole range of applied loads (19.6-127.5 N).
5) The wear rate of WC-3 coating showed a significant increase from 0.0628 to 0.191 mg.m^{-1} with the applied load ranging from 19.6 to 127.5 N, which demonstrated its lower abrasive wear resistance against alumina 60 than WC-1 and WC-2 coatings.

6. ACKNOWLEDGEMENTS

The author sincerely appreciates Professors Philip Shipway and Graham McCartney from Department of Mechanical, Materials, and Manufacturing Engineering, The University of Nottingham, UK, for their supervision, advice and encouragement throughout this research.

REFERENCES

1. Lim, N. S., Das, S., Park, S. Y., Kim, M. C., Park, C. G., "Fabrication and microstructural characterization of nano-structured WC/Co coatings", ***Surface and Coatings Technology***, Vol. 205, No. 2, (2010), 430-435. https://doi.org/10.1016/j.surfcoat.2010.07.004
2. Jia, C., Sun, L., Tang, H., Qu, X., "Hot pressing of nanometer WC-Co powder", ***International Journal of Refractory Metals and Hard Materials***, Vol. 25, No. 1, (2007), 53-56. https://doi.org/10.1016/j.ijrmhm.2005.11.003
3. Kim, H. C., Shon, I. J., Yoon, J. K., Doh, J. M., "Consolidation of ultrafine WC and WC–Co hard materials by pulsed current activated sintering and its mechanical properties", ***International Journal of Refractory Metals and Hard Materials***, Vol. 25, No. 1, (2007), 46-52. https://doi.org/10.1016/j.ijrmhm.2005.11.004
4. Bonache, V., Rayón, E., Salvador, M. D., Busquets, D., "Nanoindentation study of WC–12Co hard metals obtained from nanocrystalline powders: Evaluation of hardness and modulus on individual phases", ***Materials Science and Engineering: A***, Vol. 527, No. 12, (2010), 2935-2941. https://doi.org/10.1016/j.msea.2010.01.026
5. Li, C. J., Yang, G. J., "Relationships between feedstock structure, particle parameter, coating deposition, microstructure and properties for thermally sprayed conventional and nanostructured WC-Co", ***International Journal of Refractory Metals and Hard Materials***, Vol. 39, (2013), 2-17. https://doi.org/10.1016/j.ijrmhm.2012.03.014
6. Mateen, A., Saha, G. C., Khan, T. I., Khalid, F. A., "Tribological behaviour of HVOF sprayed near-nanostructured and microstructured WC-17wt.% Co coatings", ***Surface and Coatings Technology***, Vol. 206, (2011), 1077-1084. https://doi.org/10.1016/j.surfcoat.2011.07.075
7. Saha, G. C., Khan, T. I., "The corrosion and wear performance of microcrystalline WC-10Co-4Cr and near-nanocrystalline WC-17Co high velocity oxy-fuel sprayed coatings on steel substrate", ***Metallurgical and Materials Transactions A***, Vol. 41, No. 11, (2010), 3000–3009. https://doi.org/10.1007/s11661-010-0296-1
8. Chivavibul, P., Watanabe, M., Kuroda, S., Shinoda, K., "Effects of carbide size and Co content on the microstructure and mechanical properties of HVOF-sprayed WC–Co coatings" ***Surface and Coatings Technology***, Vol. 202, No. 3, (2007), 509-521. https://doi.org/10.1016/j.surfcoat.2007.06.026
9. Ghadami, F., Ghadami, S. and Abdollah-Pour, H., "Structural and oxidation behavior of atmospheric heat treated plasma sprayed WC–Co coatings", ***Vacuum***, Vol. 94, (2013), 64-68. https://doi.org/10.1016/j.vacuum.2013.01.019
10. Aristizabal, M., Sanchez, J. M., Rodriguez, N., Ibarreta, F., Martinez, R., "Comparison of the oxidation behaviour of WC–Co and WC–Ni–Co–Cr cemented carbides", ***Corrosion Science***, Vol. 53, No. 9, (2011), 2754-2760. https://doi.org/10.1016/j.corsci.2011.05.006
11. Zhu, Q., Zhu, H. T., Tieu, A. K., Reid, M., Zhang, L. C., "In-situ investigation of oxidation behaviour in high-speed steel roll material under dry and humid atmospheres", ***Corrosion Science***, Vol. 52, No. 8, (2010), 2707–2715. https://doi.org/10.1016/j.corsci.2010.04.027
12. Qiao, Y., Fischer, T. E., Dent, A., "The effects of fuel chemistry and feedstock powder structure on the mechanical and tribological properties of HVOF thermal-sprayed WC-Co coatings with very fine structures", ***Surface and Coatings Technology***, Vol. 172, No. 1, (2003), 24-41. https://doi.org/10.1016/S0257-8972(03)00242-1
13. Zhao, H., Ding, Z., Zhang, Y., Wang, Q., "Properties of Nanostructured WC-12Co Coatings Sprayed by HVOF", In ***Thermal Spray 2007: Global Coating Solutions (ASM International***, (2007), 884-889.

14. Schroeder, S., Melnyk, C., Grant, D., Gansert, R., Saha, G., Glenesk, L., "Properties of Powders, Coatings and Consolidated Components Produced from Nano-and Near-Nano Crystalline Powders", ***Thermal Sparay 2009: Expanding Thermal Spray Performance to New Markets and Applications***, Marple, B. R., Hyland, M. M., Lau, Y. –C., Li, C. –J., Lima, R. S., Montavon, G., Eds., ASM International, Materials Park, OH., USA, (2009), 403-408. https://doi.org/10.1361/cp2009itsc0403

15. Cho, T. Y., Yoon, J. H., Kim, K. S., Song, K. O., Joo, Y. K., Fang, W., Zhang, S. H., Youn, S. J., Chun H. G., Hwang, S. Y., "A Study on HVOF Coatings of Micron and Nano WC-Co Powders", ***Surface and Coatings Technology***, Vol. 202, No. 22-23, (2008), 5556-5559. https://doi.org/10.1016/j.surfcoat.2008.06.106

16. Stewart, D. A., Shipway, P. H., Mccartney, D. G., "Abrasive wear behaviour of conventional and nanocomposite HVOF-sprayed WC–Co coatings", ***Wear***, Vol. 225–229, (1999), 789–798. https://doi.org/10.1016/S0043-1648(99)00032-0

17. Guilemany, J. M., Dosta, S., Miguel, J. R., "The enhancement of the properties of WC-Co HVOF coatings through the use of nanostructured and microstructured feedstock powders", ***Surface and Coatings Technology***, Vol. 201, No. 3-4, (2006), 1180-1190. https://doi.org/10.1016/j.surfcoat.2006.01.041

18. Baik, K. H., Kim, J. H., Seong, B. G., "Improvements in hardness and wear resistance of thermally sprayed WC-Co nanocomposite coatings", ***Materials Science and Engineering: A***, Vol. 449-451, (2007), 846-849. https://doi.org/10.1016/j.msea.2006.02.295

19. Moore, M. A., "Abrasive Wear", in ***Treatise on Materials Science and Technology***, Scott, D., Ed., Academic Press: New York, NY, USA, (1979), p. 217-257.

20. Hewitt, S. A., Kibble, K. A., "Effects of ball milling time on the synthesis and consolidation of nanostructured WC-Co composites", ***International Journal of Refractory Metals and Hard Materials***, Vol. 27, No. 6, (2009), 937-948. https://doi.org/10.1016/j.ijrmhm.2009.05.006

21. Pang, C., Guo, Z., Luo, J., Hou, T., Bing, J., "Effect of vanadium on synthesis of WC nanopowders by thermal processing of V-doped tungsten precursor", ***International Journal of Refractory Metals and Hard Materials***, Vol. 28, No. 3, (2010), 394-398. https://doi.org/10.1016/j.ijrmhm.2009.12.006

22. Blau, P. J., ***ASM Handbook, Volume 18-Friction, Lubrication, and Wear Technology***, ASM International, (1992).

23. Park, S. Y., Kim, M. C., Park, C. G., "Mechanical properties and microstructure evolution of the nano WC–Co coatings fabricated by detonation gun spraying with post heat treatment", ***Materials Science and Engineering: A***, Vol. 449-451, (2007), 894-897. https://doi.org/10.1016/j.msea.2006.02.444

24. Guilemany, J. M., De Paco, J. M., Miguel, J. R., Nutting, J., "Characterization of the W_2C phase formed during the high velocity oxygen fuel spraying of a WC+12 Pct Co powder", ***Metallurgical and Materials Transactions A***, Vol. 30, No. 8, (1999), 1913-1921. https://doi.org/10.1007/s11661-999-0002-3

25. Wood, R. J., "Tribology of thermal sprayed WC–Co coatings", ***International Journal of Refractory Metals and Hard Materials***, Vol. 28, No. 1, (2010), 82-94. https://doi.org/10.1016/j.ijrmhm.2009.07.011

26. Watanabe, M., Owada, A., Kuroda, S., Gotoh Y., "Effect of WC size on interface fracture toughness of WC–Co HVOF sprayed coatings", ***Surface and Coatings Technology***, Vol. 201, No. 3-4, (2006), 619-627. https://doi.org/10.1016/j.surfcoat.2005.12.019

27. Kear, B. H., Skandan, G., Sadangi, R. K., "Factors controlling decarburization in HVOF sprayed nano-WC/Co hard coatings", ***Scripta Materialia***, Vol. 44, No. 8-9, (2001), 1703-1707. https://doi.org/10.1016/S1359-6462(01)00867-3

28. Fullman, R. L., "Measurement of Particle Sizes in Opaque Bodies", ***JOM-Journal of the Minerals, Metals and Materials Society***, Vol. 5, No. 3, (1953), 447-452. https://doi.org/10.1007/BF03398971

29. Di Girolamo, G., Pilloni, L., Pulci, G., Marra, F., "Tribological Characterization of WC-Co Plasma Sprayed Coatings", ***Journal of the American Ceramic Society***, Vol. 92, No. 5, (2009), 1118-1124. https://doi.org/10.1111/j.1551-2916.2009.03023.x

30. Sánchez, E., Bannier, E., Salvador, M. D., Bonache, V., García, J. C., Morgiel, J., Grzonka, J., "Microstructure and Wear Behavior of Conventional and Nanostructured Plasma-Sprayed WC-Co Coatings", ***Journal of Thermal Spray Technology***, Vol. 19, No. 5, (2010), 964-974. https://doi.org/10.1007/s11666-010-9480-5

31. Usmani, S., Sampath, S., Houck, D. L., Lee, D., "Effect of carbide particle size on the sliding and abrasive wear behavior of thermally sprayed WC-Co coatings", ***Tribology Transactions***, Vol. 40, No. 3, (1997), 470-478.

32. Sudaprasert, T., Shipway, P. H., McCartney, D. G., "Sliding wear behavior of HVOF sprayed WC-Co coatings deposited with both gas-fuelled and liquid-fuelled systems", ***Wear***, Vol. 255, No. 7-12, (2003), 943-949. https://doi.org/10.1016/S0043-1648(03)00293-x

33. Picas, J. A., Punset, M., Baile, M. T., Martin, E., Forn, A., "Properties of WC-CoCr Based Coatings Deposited by Different HVOF Thermal Spray Processes", ***Plasma Processes and Polymers***, Vol. 6, No. S1, (2009), S948-S953. https://doi.org/10.1002/ppap.200932402

34. Shaw, K. G., Gruninger, M. F., Jarosinski, W. J., "High temperature intermetallic binders for HVOF carbides", In ***1994 Thermal Spray Industrial Applications: Proceedings***, (1994).

35. Schwetzke, R., Kreye, H., "Microstructure and properties of tungsten carbide coatings sprayed with various high-velocity oxygen fuel spray systems", ***Journal of Thermal Spray Technology***, Vol. 8, No. 3, (1999), 433-439. https://doi.org/10.1361/105996399770350395

36. Stewart, D. A., Shipway, P. H., McCartney, D. G., "Microstructural evolution in thermally sprayed WC-Co coatings: comparison between nanocomposite and conventional starting powders", ***Acta Materialia***, Vol. 48, No. 7, (2000), 1593-1604. https://doi.org/10.1016/S1359-6454(99)00440-1

37. Ban, Z. G., Shaw, L. L., "Characterization of thermal sprayed nanostructured WC-Co coatings derived from nanocrystalline WC-18wt.% Co powders", ***Journal of Thermal Spray Technology***, Vol. 12, No. 1, (2003), 112-119. https://doi.org/10.1361/105996303770348564

38. Ishikawa, Y., Kuroda, S., Kawakita, J., Sakamoto, Y., Takaya, M., "Sliding Wear Properties of HVOF Sprayed WC-20% Cr3C2-7% Ni Cermet Coatings", ***Surface and Coatings Technology***, Vol. 201, No. 8, (2007), 4718-4727. https://doi.org/10.1016/j.surfcoat.2006.10.007

39. Rodriguez, M., Klisans, J., Bavaresco, L., Scagni, A., Arenas, F., "Wear resistance of HVOF sprayed carbide coatings", In ***Thermal Spray 2001: New Surfaces for a New Millennium, Proceedings, International Thermal Spray Conference (ITSC 2001), Singapore,*** 28- 30 May, (2001), 1061-1068.

40. Hutchings, I. M., "Tribology: Friction and Wear Engineering Materials", Ed. Edward Arnold, a Division of Hodder Headline PLC., (1992), 273.

41. Nahvi, S. M., Shipway, P. H., McCartney, D. G., "Particle motion and modes of wear in the dry sand-rubber wheel abrasion test", ***Wear***, Vol. 267, No. 11, (2009), 2083-2091. https://doi.org/10.1016/j.wear.2009.08.013

42. Stevenson, A. N. J., Hutchings, I. M., "Development of the dry sand rubber wheel abrasion test", ***Wear***, Vol. 195, No. 1-2, (1996), 232-240. https://doi.org/10.1016/0043-1648(96)06965-7

43. Tylczak, J. H., Hawk, J. A., Wilson, R. D., "A comparison of laboratory abrasion and field wear results", ***Wear***, Vol. 225-229, No. 2, (1999), 1059-1069. https://doi.org/10.1016/S0043-1648(99)00043-5

44. Blombery, R. I., Perrot, C. M., Robinson, P. M., "Abrasive wear of tungsten carbide-cobalt composites. I. Wear mechanisms", ***Materials Science and Engineering***, Vol. 13, No. 2, (1974), 93-100. https://doi.org/10.1016/0025-5416(74)90176-1

45. Chen, H., Xu, C., Zhou, Q., Hutchings, I. M., Shipway, P. H., Liu, J., "Micro-scale abrasive wear behaviour of HVOF sprayed and laser-remelted conventional and nanostructured WC-Co coatings", ***Wear***, Vol. 258, No. 1-4, (2005), 333-338. https://doi.org/10.1016/j.wear.2004.09.044

46. Lee, H. C., Gurland, J., "Hardness and deformation of cemented tungsten carbide", ***Materials Science and Engineering***, Vol. 33, No. 1, (1978), 125-133. https://doi.org/10.1016/0025-5416(78)90163-5

47. Nahvi, S. M., "Investigating the Abrasive Wear Resistance of Thermal-Sprayed WC-Based Coatings", ***Advanced Ceramics Progress***, Vol. 6, No. 2, (2020), 7-16. https://doi.org/10.30501/ACP.2020.107360